Geophysical Journal International

Geophys. J. Int. (2010) **180,** 418–432 doi: 10.1111/j.1365-246X.2009.04427.x

An adaptive smoothing algorithm in the TSN modelling of rupture propagation with the linear slip-weakening friction law

Martin Galis,[1] Peter Moczo,[1] Jozef Kristek[1] and Miriam Kristekova[2]

[1]*Faculty of Mathematics, Physics and Informatics, Comenius University Bratislava, Mlynska dolina F1,* 842 48 *Bratislava, Slovak Republic.*
E-mail: moczo@fmph.uniba.sk
[2]*Geophysical Institute, Slovak Academy of Sciences, Dubravska cesta* 9, 845 28 *Bratislava, Slovak Republic*

Accepted 2009 October 21. Received 2009 July 23; in original form 2009 April 17

SUMMARY

We present an adaptive smoothing algorithm for reducing spurious high-frequency oscillations of the slip-rate time histories in the finite-element (FE)–traction-at-split-node modelling of dynamic rupture propagation on planar faults with the linear slip-weakening friction law. The algorithm spatially smoothes trial traction on the fault plane. The smoothed value of the trial traction at a gridpoint and time level is calculated if the slip is larger than 0 simultaneously at the gridpoint and eight neighbouring gridpoints on the fault. The smoothed value is a weighted average of the Gaussian-filtered and unfiltered values. The weighting coefficients vary with slip.

Numerical tests for different rupture propagation conditions demonstrate that the adaptive smoothing algorithm effectively reduces spurious high-frequency oscillations of the slip-rate time histories without affecting rupture time. The algorithm does not need an artificial damping term in the equation of motion.

We implemented the smoothing algorithm in the FE part of the 3-D hybrid finite-difference (FD)–FE method. This makes it possible to efficiently simulate dynamic rupture propagation inside a FE subdomain surrounded by the FD subdomain covering major part of the whole computational domain.

Key words: Numerical solutions; Earthquake dynamics; Computational seismology.

GJI Seismology

1 INTRODUCTION

The importance of the numerical simulation of the dynamic rupture propagation in investigating physics of earthquakes is evident from many recent theoretical and application studies as well as validation projects and efforts (e.g. Harris & Archuleta 2004; Harris *et al.* 2004, 2009; Moczo *et al.* 2005, 2006).

Dynamic representations of the rupturing fault have been implemented in different formulations of the, for example, finite-difference (FD) method (e.g. Andrews 1973, 1976a,b, 1999; Madariaga 1976; Day 1977, 1982; Miyatake 1980; Madariaga *et al.* 1998; Nielsen *et al.* 2000; Cruz-Atienza & Virieux 2004; Day *et al.* 2005, Dalguer & Day 2006, 2007; Moczo *et al.* 2007a; Rojas *et al.* 2008; for a brief review of the FD implementations see Moczo *et al.* 2007b), FE method (e.g. Archuleta 1976; Archuleta & Frazier 1978; Oglesby *et al.* 1998, 2000; Oglesby 1999; Aagaard *et al.* 2001; Anderson *et al.* 2003; Ma & Archuleta 2006; Ma 2008; Ma *et al.* 2008), boundary-integral method (e.g. Das 1980; Andrews 1985; Cochard & Madariaga 1994; Aochi *et al.* 2000; Lapusta *et al.* 2000; Lapusta & Rice 2003; Day *et al.* 2005) or spectral-element method (e.g. Ampuero 2002, 2008; Festa 2004; Vilotte *et al.* 2006; Chaljub *et al.* 2007; Kaneko *et al.* 2008).

The traction-at-split-node (TSN) method, developed independently by Andrews (1973, 1999) and Day (1977, 1982), seems to be the most suitable method to represent the fault discontinuity in the FD and FE methods. Recently, Day *et al.* (2005) found very good level of agreement between the FD implementation of the TSN method (on partly staggered grid; called DFM in their paper) with the boundary integral method. Moreover, Dalguer & Day (2006) demonstrated superior accuracy of the TSN method compared to the thick-fault (Madariaga *et al.* 1998) and stress-glut method (presented by Andrews 1999).

Despite the superior properties of the TSN method, its implementations in the low-order approximation discrete methods are not free from problems. In this paper, we focus on spurious high-frequency oscillations often seen in the slip-rate time histories. We start with general considerations.

For a given initial stress and material parameters on the fault, it is the friction law that controls initialization, propagation and healing of the rupture. Consider Coulomb friction law (Fig. 1a). The stress is discontinuous at the crack tip, that is at the point of the fault at the rupture arrival time t_r. According to the left-hand value, corresponding to the static friction, the point of the fault at the crack tip should be at rest. According to the right-hand value,

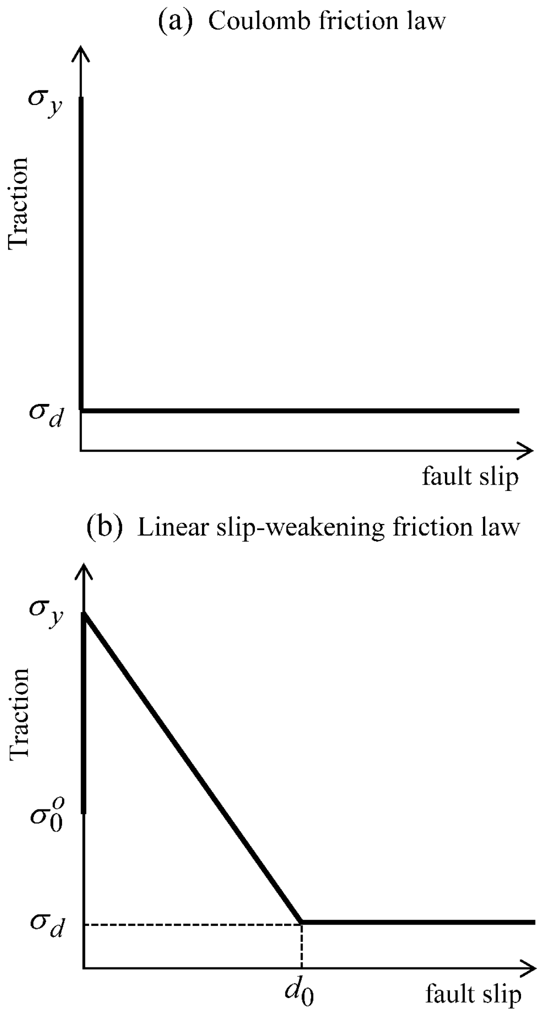

Figure 1. (a) Coulomb friction law. (b) Linear slip-weakening friction law. σ_y – static traction, σ_d – dynamic traction, σ_0^o – initial traction and d_0 – critical slip.

corresponding to the dynamic friction, the point of the fault at the crack tip should be slipping. This implies an infinitely large slip rate at the crack tip, that is at time t_r at a point of the fault. The slip-rate value then rapidly decreases with time. The narrow pulse of slip rate with the infinite peak value implies infinitely broad spectrum and thus also very high frequencies.

Consider a linear slip-weakening friction law (Fig. 1b). The gradual decrease of stress (during finite time and finite slip) removes infinite value of the slip rate at the crack tip, at time t_r (compared to the Coulomb friction law). The slip rate increases from zero value at t_r. The steeper is the decrease of the stress in the friction law, the steeper is the increase of the slip rate, and, consequently, the broader is the spectrum of shear stress and slip rate variations generated by the slipping point.

The gradual decrease of the stress at a slipping point implies the existence of the breakdown zone. The breakdown zone is the spatial zone on the fault plane behind the crack tip where the shear stress decreases from its static value to its dynamic value. Consequently, also the slip rate varies significantly in the breakdown zone.

Thus a possibly broad-spectrum slip-rate and stress variations generated by each slipping point as well as the spatial breakdown zone have to be properly discretized in a numerical method in order to avoid effect of numerical grid dispersion at higher frequencies and to properly capture the stress degradation in the breakdown zone.

In the wave propagation problems a size of the spatial grid spacing (for a given order of approximation in a chosen numerical method) determines how accurately high frequencies will be propagated by a grid. An effect of the numerical grid dispersion, proportional to a travel path length, may become considerable/visible for wavelengths shorter than a certain value.

In the rupture propagation problems an effect of the numerical grid dispersion may become more dramatic due to the coupling between the shear stress and slip rate. In the TSN method a slip-rate increment at each time level is calculated from the difference between the so-called trial traction (value of the constraint traction assuring zero slip rate) and frictional traction at a point of the fault. Whereas the frictional traction itself does not suffer from oscillations (it is determined by the friction law), the trial traction is not smooth in time reflecting the presence of the high-frequency stress variations inaccurately propagated by the grid. The inaccurately determined slip-rate increment is used in calculation of the slip rate in the next time level causing oscillations of the slip rate which in turn affects the value of the trial traction.

Thus for a given friction law (for a given steepness of the stress decrease) and order of approximation in the applied numerical method it is the size of the spatial grid spacing that determines how accurately high frequencies will be propagated by a grid and how large the high-frequency oscillations of the slip rate will be.

Likely in most practical applications the spatial sampling will not be fine enough to prevent visible spurious oscillations in the low-order approximation numerical method.

If the oscillations do not affect (change) development and propagation of the rupture, it is possible to apply *a posteriori* low-pass filtration to remove the oscillations. The problem is that a priori we cannot in principle assume that the oscillations would not change the development and propagation of the rupture. Therefore, the low-pass filtration cannot serve as a systematic tool for reducing the oscillations.

Day (1982), Day & Ely (2002), Day *et al.* (2005) and Dalguer & Day (2007) applied an added artificial viscosity in their implementations of the TSN method to regularize the numerical solution and suppress the spurious oscillations. They added terms to the equations of motion that are proportional to the strain-rate components. This leads to damping stresses of Kelvin–Voigt form characterized by a damping parameter. The damping is scale selective, with the scale set by the size of the grid spacing. The sensitivity to the damping parameter diminishes with increasing number of gridpoints per breakdown zone. Whereas Day (1982), Day & Ely (2002) and Day *et al.* (2005) applied the artificial damping throughout the volume in the FD scheme on the partly staggered grid, Dalguer & Day (2007) included the damping term only in the equations of motion for the split nodes in the staggered-grid FD scheme. In both cases Day *et al.* found preferred values of the damping parameters for numerical simulations, and, consequently, local criteria for spatial sampling of the breakdown zone. Although both TSN implementations (DFM—the discrete fault model on the partly staggered grid, and SGSN—the staggered-grid split node method) converge even with no artificial damping applied, the application of the damping with proper values of the damping parameter greatly accelerates the convergence. The artificial damping reduces the rupture time error and spurious oscillations in the slip-rate time histories if a proper value of the damping parameter is used. However, the peak slip-rate misfit increases with damping (having minimum if no damping is applied).

In this paper, we present an alternative approach to suppress spurious oscillations of the slip rate. We do not introduce any artificial damping term in the equation of motion. The basic idea of our approach is to spatially smooth the trial traction before it is used in calculation of the slip-rate increment.

We restrict our study to the linear slip-weakening friction law. We know from our unpublished numerical results that the slip-rate history for friction law by Ohnaka & Yamashita (1989) is considerably smoother compared to the linear slip-weakening friction law. The very recent study by Rojas *et al.* (2009) shows that the slip-rate oscillations are less of a problem in the rate-and-state friction laws than in the linear slip-weakening friction law, because of a natural damping inherent in the friction law.

We first very briefly present the FD–FE hybrid method used for numerical simulations. Then we continue with considerations on smoothing the trial traction. We continue with defining problem configurations for simulations of rupture propagation. In the next section, we present results of extensive numerical tests aiming to find the best smoothing algorithm. Finally, we demonstrate the performance of the preferred smoothing algorithm.

2 THE FINITE-DIFFERENCE–FINITE-ELEMENT HYBRID METHOD

The numerical simulations were performed using the 3-D hybrid FD–FE method. The method was presented in detail by Galis *et al.* (2008). Here we just briefly summarize its principle and main features. The method is based on a combination of the fourth-order velocity–stress staggered-grid FD scheme with the second-order displacement FE method. A computational domain can include one or several relatively small FE subdomains whereas a major part of the whole computational domain is covered by a FD grid. The FD and FE parts causally communicate at each time level in the FD–FE transition zone. The transition zone consists of the FE Dirichlet boundary, FD–FE averaging zone and FD Dirichlet zone. The structure of the FD–FE transition zone is the key aspect of the hybrid combination.

The FE subdomains can comprise extended kinematic or dynamic models of the earthquake source or the free-surface topography. The TSN method is implemented in the FE method for simulation of the spontaneous rupture propagation. A detailed exposition of the implementation of the TSN method is given in the monograph by Moczo *et al.* (2007a).

Let us briefly mention the aspect of the numerical integration within an element. We can use 8-point Gauss integration or 8-point Lobatto integration in the FE algorithm. Because we use hexahedra elements with trilinear shape functions, 8-point Gauss integration is full integration while 8-point Lobatto integration is a reduced integration. The 8-point Lobatto integration would be exact in the case of the linear shape functions, similarly as the 1-point Gauss integration would be in this case. With reduced 8-point Lobatto integration it is not necessary to apply stabilization which would be necessary with the 1-point Gauss integration; for details see Ma & Liu (2006). In our numerical simulations we applied the 8-point Lobatto integration.

The key feature of the computational efficiency of the hybrid method is the fact that in many problems the FD method can be applied to a major part of the computational domain. In addition to this, the computational efficiency of the implemented FE formulation itself is based on two approaches: (1) the use of the global restoring-force vector significantly reduces memory requirements compared to the standard formulation based on the global stiffness matrix and (2) the use of new base functions allows employing new effective parameters which eliminate redundant information in the standard way of the restoring-force computation. The elimination leads to the considerable reduction of the number of arithmetic operations and thus to reduction of the computational time. The new base functions and effective parameters for a 2-D problem are described by Balazovjech & Halada (2007) and Moczo *et al.* (2007a). A detailed 3-D theory will be presented in a separate study.

The numerical simulations used in this study included a rupturing fault plane inside the FE subdomain.

3 SMOOTHING ALGORITHM–BASIC CONSIDERATIONS

We want to spatially (on the fault plane) smooth the trial traction. This can be achieved by averaging values of the trial traction at gridpoints in some neighbourhood of the gridpoint at which the smoothed value is to be calculated. In principle there are two questions: (1) When or under which conditions the averaging should be applied? (2) How to average? Here we outline preliminary considerations which led us to definition of alternative smoothing algorithms. The algorithms and the numerical tests will be detailed later.

Obviously, an extreme possibility is to apply averaging over the entire fault plane at each time level, that is, unconditionally. Intuitively we can anticipate that such averaging should be capable to smooth the slip-rate time history. At the same time, however, such averaging would be insensitive and robust—the unconditional averaging might smooth the onset of the slip too much and thus likely affect development of the rupture.

It seems more reasonable and natural to condition the averaging at a gridpoint by some criterion. The averaging should not affect the onset of the slip. Therefore, the averaging should not be applied at the rupture front. The application to a slipping point should be conditioned by a threshold value of slip or slip rate. The threshold condition can be required only at a gridpoint or simultaneously at the point and neighbouring gridpoints; the two possibilities differ in the way of identifying the rupture front. The application of the threshold condition to slip or slip-rate might depend on the adopted friction law.

The averaging formula should allow for tuning and possibly also for defining an adaptive smoothing that might reflect development of the rupture. We define it as follows. Let p be the averaging parameter, and

$$0 \le p \le 1. \tag{1}$$

Then the weighted averaging can be expressed by

$$\bar{\bar{\vec{T}}}(i,j) \;=\; (1-p)\;\vec{T}(i,j) \;+\; p\vec{T}_G(i,j). \tag{2}$$

Here $\bar{\bar{\vec{T}}}(i,j)$ is the smoothed trial traction at the gridpoint (i, j), $\vec{T}(i,j)$ is the original trial traction and $\vec{T}_G(i,j)$ is obtained from

$$\vec{T}^G(i,j) = \sum_{k=1}^{3}\sum_{l=1}^{3} w_{kl}^G\,\vec{T}(i+k-2, j+l-2), \tag{3}$$

where

$$w^G = \begin{bmatrix} 1/16 & 1/8 & 1/16 \\ 1/8 & 1/4 & 1/8 \\ 1/16 & 1/8 & 1/16 \end{bmatrix}. \qquad (4)$$

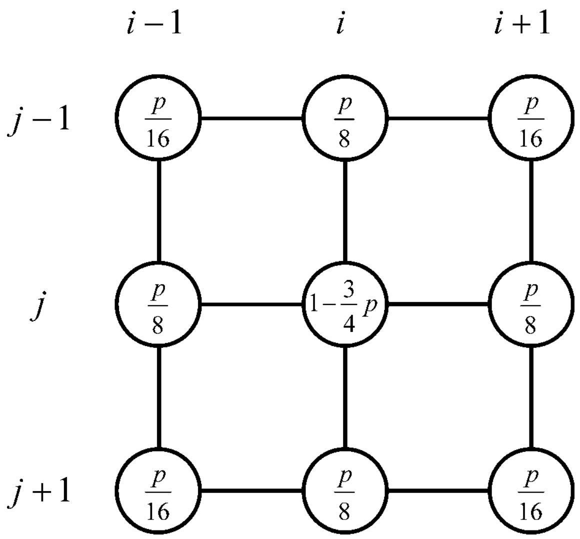

Figure 2. Scheme of the effective weighting coefficients in the adaptive smoothing algorithm for calculation of the trial traction at grid position (i, j) on the fault plane. The weighting factor $p \in \langle 0, 1\rangle$ and may vary with time.

Note that elements of matrix w^G are coefficients of the Gaussian filter. Eq. (2) can be rewritten in the form

$$\bar{\bar{\vec{T}}}(i, j) = \sum_{k=1}^{3} \sum_{l=1}^{3} \bar{w}_{kl}\, \vec{T}(i + k - 2, j + l - 2) \qquad (5)$$

with

$$\bar{w} = \begin{bmatrix} p/16 & p/8 & p/16 \\ p/8 & 1 - 3p/4 & p/8 \\ p/16 & p/8 & p/16 \end{bmatrix}. \qquad (6)$$

The averaging coefficients are illustrated in Fig. 2.

4 PROBLEM CONFIGURATIONS

In order to develop and test a desired smoothing algorithm we numerically simulate spontaneous rupture propagation for two configurations of a planar fault embedded in a uniform infinite elastic isotropic space. Configuration 1 is a modified Version 3 of the Southern California Earthquake Center (SCEC) benchmark problem (Harris *et al.* 2004; Day *et al.* 2005; Dalguer & Day 2007). The modification consists in different definition of the initialization zone (as it will be detailed later). We use Configuration 1 for developing a preferred smoothing algorithm.

The Configuration 1 geometry is shown in Fig. 3. The fault plane is the xy-plane and the origin of the coordinate system is located in the middle of the rupture-allowed area. The initial shear traction is aligned with the x-axis. The x- and y-axes are axes of symmetry or antisymmetry for the fault slip and traction components. Consequently, the xz-plane is restricted to purely in-plane motion whereas the yz-plane to purely antiplane motion.

Rupture is allowed within a fault area that extends 30 and 15 km in the x- and y-directions, respectively. Spatially constant P- and

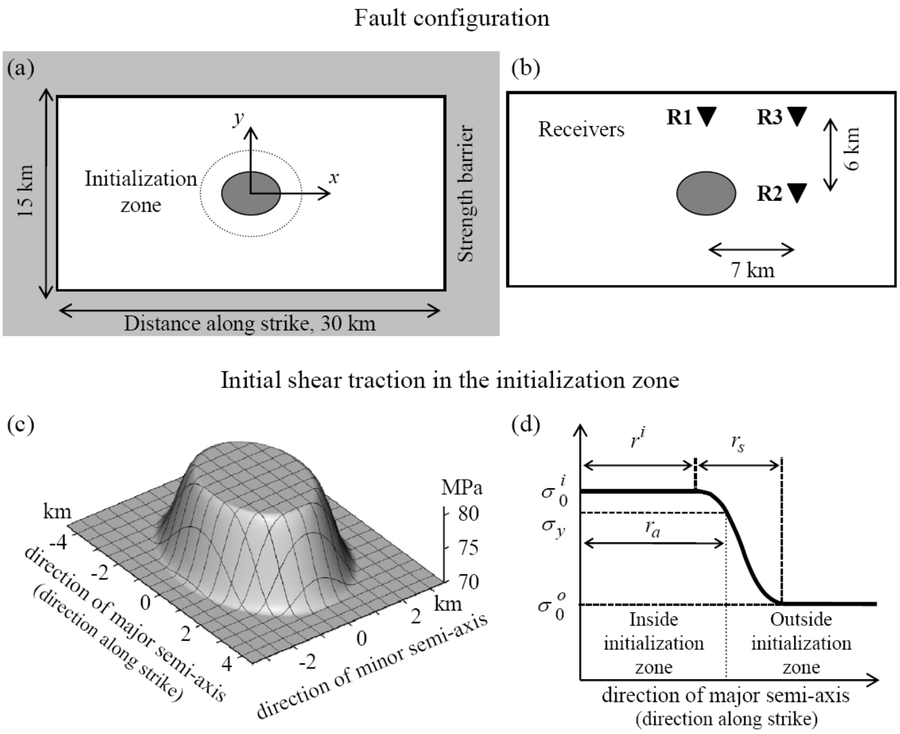

Figure 3. (a) Geometry of the rupture-allowed area and initialization zone. (b) Positions of the antiplane receiver R1, in-plane receiver R2 and mixed-position receiver R3. (c) 3-D visualization of the initial shear traction in the initialization zone. (d) Initial traction along the strike position. σ_y is the static traction.

Table 1. Dynamic stress parameters for initialization and spontaneous dynamic rupture simulation. RAA—Rupture Allowed Area, SB—Strength Barrier.

				Config. 1	Config. 2
		Linear slip weakening			
Static coeff.	RAA	μ_s		0.6778	0.6125
of friction	SB	μ_s		10 000	10 000
Dynamic coeff. of friction		μ_d		0.525	0.525
Critical slip		d_0	[m]	0.4	0.275
Static traction		$\sigma_y = \mu_s \cdot \sigma_n 0$	[MPa]	81.333	73.5
Dynamic traction		$\sigma_d = \mu_d \cdot \sigma_n 0$	[MPa]	63	63
		Initial stress			
Initial shear stress outside the initialization zone		σ_0^o	[MPa]	70	70
Initial normal stress		$\sigma_n 0$	[MPa]	−120	−120
Stress drop		$\Delta\tau = \sigma_0^o - \sigma_d$	[MPa]	7	7
Strength parameter		S		1.62	0.50
Strength excess		$\Delta\sigma_y = \sigma_y - \sigma_0^o$	[MPa]	11.333	3.500
		Initialization			
Size of the	Major semi-axis	r_a	[m]	2035	1089
initialization zone	Minor semi-axis	r_b	[m]	1526	817
Overshoot		ε_σ	[% of $\Delta\sigma_y$]	0.06765	0.06765
			[MPa]	7.667×10^{-3}	2.368×10^{-3}
Max. value of the σ_0^2 initial shear stress inside the initialization zone		$\sigma_0^i = \sigma_y + \varepsilon_\sigma$	[MPa]	81.341	73.502
Semi-major axis of the ellipse with σ_0^i		r^i	[m]	2010.02	1064.53
Width of the smooth transition zone of the initial stress		r_s	[m]	1500	1500

S-wave velocities and density are 6000 m s^{-1}, 3464 m s^{-1} and 2670 kg m^{-3}. The dynamic stress parameters for initialization and spontaneous rupture propagation are given in Table 1 and the linear slip-weakening friction law is illustrated in Fig. 4. The initialization zone has elliptical shape and is located in the middle of the rupture-allowed area as shown in Fig. 3(a). The major semi-axis r_a and minor semi-axis r_b are determined as critical half-lengths $L_{c\mathrm{II}}$ and $L_{c\mathrm{III}}$ (Andrews 1976a,b) for the in-plane and antiplane modes, respectively. The elliptical initialization zone enables a smooth spatial transition between the shear traction inside and outside the initialization zone as it is detailed in Figs 3(c) and (d) and Table 1. The rupture is simultaneously initiated due to the initial shear traction slightly higher than the static traction in the initialization zone (by 0.06765 per cent of the strength excess). After this initialization the rupture propagates spontaneously following the linear slip-weakening friction law.

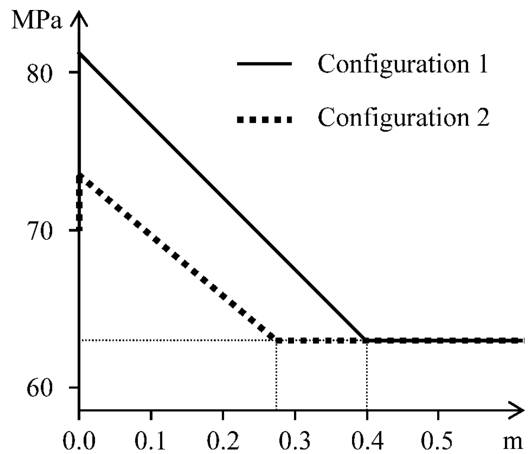

Figure 4. Linear slip-weakening friction laws for the two considered configurations.

Configuration 2 is a modification of Configuration 1. The purpose of the modification was to allow for a rather different rupture propagation condition, namely the supershear rupture propagation. Parameters of the configuration are given in Table 1, the linear slip-weakening friction law is shown in Fig. 4. Note the values of r_a and r_b for Configuration 2. We had to use $r_a = 1.36L_{c\mathrm{II}}$ and $r_b = 1.36L_{c\mathrm{III}}$ in order to initialize spontaneous rupture propagation (the increasing of the overshoot did not lead to a proper initialization).

We can briefly comment on the values of r_a and r_b for both configurations. We found that the estimates for 2-D problem (Andrews 1976a,b) are sufficient for the 3-D Configuration 1. Therefore, we applied the trial and error procedure to find proper values for the 3-D Configuration 2. The found values of r_a and r_b are smaller than the estimate for the circular initialization zone according to Day (1982).

The geometrical configuration of the rupturing fault in the computational domain is illustrated in Fig. 5. The FE subdomain is covered by a uniform grid of cubic elements with size h_{FE}, the FD subdomain is covered by a uniform grid with grid spacing $h_{\mathrm{FD}} = 2h_{\mathrm{FE}}$. All simulations are referred to according to the size of the cubic element in the FE subdomain. For example, '$h = 50$ m' will refer to the simulations with $h_{\mathrm{FE}} = 50$ m. Table 2 lists all spatial discretizations used in numerical simulations. The left-hand column shows how the particular discretization will be referred to in the text.

5 EVALUATION OF THE NUMERICAL RESULTS

We present results of the numerical simulations using (1) plots of the slip-rate time histories at the antiplane receiver R1, in-plane

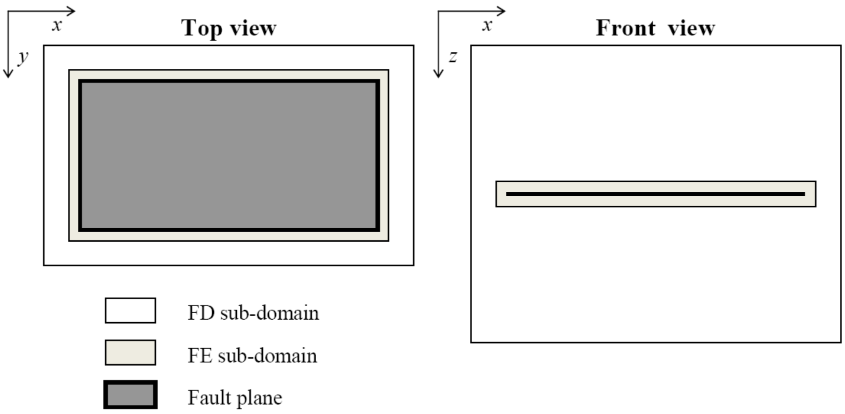

Figure 5. Schematic illustration of the geometrical configuration of the rupturing fault in the computational domain for the size of element in the FE subdomain $h_{\mathrm{FE}} = 50\,\mathrm{m}$.

Table 2. h_{FE}, size of element in the FE subdomain; h_{FD}, size of grid spacing in the FD subdomain; Δt, time step; N_{FE}, number of elements in the FE subdomain; N_{FD}, number of grid cells in the FD subdomain; M_{FE}, number of elements if the whole computational domain would be solved by the FEM.

	h_{FE} (m)	h_{FD} (m)	Δt (s)	N_{FE}	N_{FD}	M_{FE}
$h = 50$ m	50	100	0.0033	11 520 000	25 040 000	198 200 000
$h = 75$ m	75	150	0.005	5 630 000	13 090 000	103 330 000
$h = 100$ m	100	200	0.0066	3 470 000	3 440 000	26 960 000
$h = 150$ m	150	300	0.0099	2 250 000	1 230 000	9 530 000
$h = 250$ m	250	500	0.016	890 000	390 000	3 000 000
$h = 300$ m	300	600	0.02	700 000	250 000	1 900 000

receiver R2, and mixed-position receiver R3 shown in Fig. 3(b), (2) root mean square average over the fault plane of the apparent rupture velocity differences between compared solutions, (3) contour plots of the rupture front, (4) breakdown zone spatial resolution in the antiplane direction.

In all cases we consider the rupture time $t_r(x, y)$ as the time at which the slip rate first exceeds 1 mm s^{-1}. The absolute value of the rupture velocity at a point of the fault, $|\, v_r(x, y)\,|$, is determined through the rupture slowness $s_r(x, y)$

$$s_r(x, y) = grad[t_r(x, y)], \tag{7}$$

$$|v_r(x, y)| = |s_r(x, y)|^{-1}. \tag{8}$$

Because we have to expect numerical errors in evaluation of $|v_r(x, y)|$ in the discrete space–time grid, it is reasonable to spatially smooth value of $|v_r(x, y)|$. We apply the Gaussian filter (see eq. (4)).

The root mean square (rms) average of differences in the rupture velocities between two solutions is evaluated over the shadowed area (say rupture evaluation area, REA) shown in Fig. 6. For Configuration 1, the major and minor semi-axes of the inner ellipse are $(2035 + 1500)$ m $=$ 3535 m and $(1526 + 1500 \times 1526/2035)$ m $=$ 2650 m, respectively. The major and minor semi-axes of the outer ellipse are 15500 and 8500 m. For Configuration 2 the evaluation area is reduced using four ellipses with major and minor semi-axes equal to 4000 and 1800 m, respectively. An angle between the x-axis and the major axis of the additional ellipse is 40°.

The removal of the areas is necessary because small differences in positions of intersection of the original and bifurcating rupture fronts in two solutions lead to large errors in the rms differences. These errors are not due to different rupture velocities. Therefore,

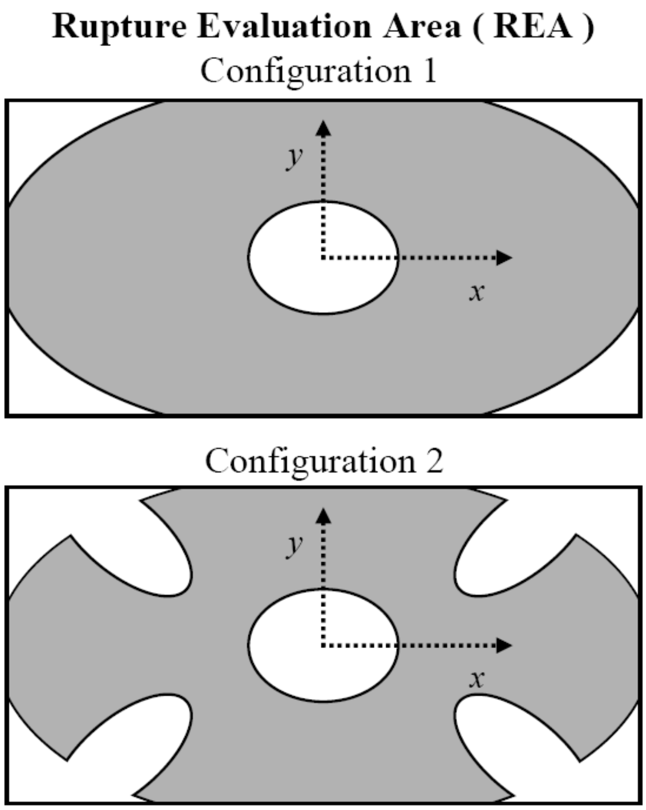

Figure 6. Geometry of the fault area used in evaluation of the numerical results for the two problem configurations.

the evaluation of the rms misfit also in the removed areas would lead to meaningless values.

The rms misfit between one solution and the solution considered as reference is evaluated as

$$\mathrm{rms} = \sqrt{\frac{\sum\left[\left|v_r(x,y)\right|_{\mathrm{GF}} - \left|v_r^{\mathrm{REF}}(x,y)\right|_{\mathrm{GF}}\right]^2}{\sum\left[\left|v_r^{\mathrm{REF}}(x,y)\right|_{\mathrm{GF}}\right]^2}} \times 100\,\text{per cent}, \tag{9}$$

where the summation relates to the gridpoints within the REA and subscript GF denotes Gaussian-filtered values.

If we know the rupture time and time when shear traction reaches level of the dynamic friction at each gridpoint along the chosen direction, we can determine a breakdown-zone spatial resolution along the chosen direction of the rupture propagation. We can also visualize the breakdown zone in a graph with one axis corresponding to the spatial coordinate along the chosen direction and one axis corresponding to time. Because the width of the breakdown zone varies with distance, we follow Day *et al.* (2005) and Dalguer & Day (2007), and evaluate an average breakdown-zone spatial resolution as a spatial resolution of a median of the breakdown-zone widths at all gridpoints along the chosen direction of rupture propagation.

Day *et al.* (2005) and Dalguer & Day (2007) evaluated the breakdown-zone resolution for the in-plane direction. They chose the in-plane direction because the rupture propagates in this direction to longer distances which means larger number of gridpoints. If we, however, evaluate the rms rupture velocity misfit over the REA and relate it to the spatial grid spacing and breakdown-zone spatial resolution, we should not bias this relation by inaccuracy due to insufficient spatial resolution of the narrowest breakdown zone. In our simulations the minimum resolution and average resolution for the antiplane direction are smaller than those in the in-plane direction. Therefore we consider the antiplane direction for evaluation of the breakdown-zone resolution in relation to the size of the grid spacing and rms misfit. Thus, $\bar{N}_b$ will be used later to denote the median breakdown-zone resolution evaluated for the antiplane direction.

6 SMOOTHING ALGORITHM

Fig. 7 summarizes all numerically tested smoothing algorithms. Algorithm A: unconditional averaging of the trial traction over the entire fault plane at each time level. The averaging is applied at a point of the fault even after the slipping ceases at the point. Algorithm B: averaging at a point of the fault is applied if a specified condition on the slip rate (B1, B2) or slip (B3) is satisfied at the point. Algorithm C: averaging at a point of the fault is applied if a specified condition on the slip rate (C1, C2) or slip (C3, C4) is satisfied simultaneously at the point and 8 neighbouring gridpoints on the fault. Further we explain the numerical tests and search for the preferred smoothing algorithm in detail.

Algorithm A. As it is specified in Fig. 7, we performed seven ($N = 7$) numerical simulations. The unconditional averaging was applied in each of them for different value of parameter $p = p_{\max}$ (see two rightmost columns in Fig. 7). There is no averaging if $p = p_{\max} = 0$, whereas $p = p_{\max} = 1$ corresponds to the strongest, pure Gaussian filtering, see eq. (2). The larger $p_{\max}$ is, the smoother is the slip rate. The solutions strongly depend on the value of parameter $p_{\max}$ and differ considerably in the rupture time and peak value. The obtained results for the antiplane receiver R1 and in-plane receiver R2 are illustrated in Fig. 8. The grey area shows the scatter of all seven solutions. Its upper border represents maximum slip rate from the seven solutions at each time, the lower border minimum slip rate. Only two slip-rate time histories are shown explicitly—the non-smoothed ($p = p_{\max} = 0$) and the smoothed one for $p = p_{\max} = 0.4$. We conclude that the algorithm A is not a proper tool for smoothing slip rate.

Algorithm B. In algorithm B we introduce parameter Q which is either slip rate (in B1 and B2) or the ratio of the slip and the critical slip (in B3).

In B1 the averaging at a point of the fault is applied if Q, the slip rate at the point, is larger than $Q_{\mathrm{thr}} = Q_{\max}$. We performed simulations for five ($N = 5$ in Fig. 7) different values of $Q_{\mathrm{thr}} = Q_{\max}$ and $p = p_{\max} = 0.4$. The solutions are similar to those obtained with algorithm A. We do not show them in Fig. 8.

In B2 the averaging parameter p increases linearly from 0 for the slip rate equal to Q_{thr} up to $p_{\max}$ for the slip rate equal to $Q_{\max}$, see the rightmost column in Fig. 7. We performed 2 simulations differing in values of parameters Q_{thr} and $Q_{\max}$. The solutions are very close to those obtained with algorithm B1. We do not show them in Fig. 8.

In B3 the averaging at a point of the fault is applied if Q, the slip-to-critical slip ratio at the point, is larger than $Q_{\mathrm{thr}} = Q_{\max}$. We performed six simulations differing in value of parameter $Q_{\mathrm{thr}} = Q_{\max}$ (in all we used $p = p_{\max} = 0.4$). The solutions are almost identical to those obtained with algorithm B1. The smoothness of the slip-rate curve and rupture time considerably depend on Q_{thr} especially at the antiplane receiver R1. The solutions obtained with algorithm B3 are illustrated in Fig. 8. The grey area indicates the scatter of the obtained solutions in the same way as in the case of algorithm A. Explicitly shown are the non-smoothed solution and the smoothed solution for $Q_{\mathrm{thr}} = Q_{\max} = 1/2$. We conclude that the algorithm B is not a proper tool for smoothing slip rate.

Algorithm C. The only but substantial difference between B1–B3 and C1–C3 algorithms, respectively, is that the condition on the slip rate or the slip-to-critical slip ratio has to be satisfied simultaneously at the point and eight neighbouring gridpoints on the fault. The structure of the performed numerical tests with the C1–C3 algorithms is the same as that with the B1–B3 algorithms, see Fig. 7.

The solutions obtained with C1 considerably depend on Q_{thr} at the antiplane receiver R1 and much less at the in-plane receiver R2, where the rupture times are relatively good. The solutions are not shown in Fig. 8.

As in B2, also in C2 the averaging parameter p varies linearly from 0 for the slip rate equal to Q_{thr} up to $p_{\max}$ for the slip rate equal to $Q_{\max}$. Solutions are comparable with those obtained with algorithm C1. The solutions are not shown in Fig. 8.

Contrary to C1 and C2, in C3 the threshold criterion is applied to the slip-to-critical slip ratio. The solutions are illustrated in Fig. 8. The grey areas for R1 and R2 indicate that the scatter of solutions due to different values of $Q_{\mathrm{thr}} = Q_{\max}$ is similar in the antiplane and in-plane receivers. However, at the antiplane receiver R1 the rupture times of the smoothed solutions are smaller than the rupture time of the non-smoothed solution, whereas at the in-plane receiver R2 it is just opposite. The time advance at R1 and delay at R2 increase with the size of the grid spacing.

The numerical results obtained with algorithms A, B and C1–C3 lead us to conclude that it is better to apply a threshold criterion simultaneously at a point and eight neighbouring gridpoints on the fault, use slip for the threshold criterion, and adjust value of the averaging parameter p to the slip development. The reason why the slip is better quantity for a threshold criterion than the slip rate can be explained in view of the applied friction law. While it is

Code	TC	Q	N	Q_{thr}	Q_{max}	p_{max}	$p\,(Q)$
A	N/A	N/A	7	N/A	N/A	0.0, 0.1, 0.2, 0.4, 0.7, 0.8, 1.0	$p = p_{max} = const.$
B1	1-point	slip rate [m/s]	5	0.0, 0.001, 0.5, 0.75, 1.0		0.4	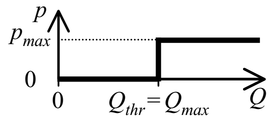
B2	1-point	slip rate [m/s]	2	0.0	0.5	0.4	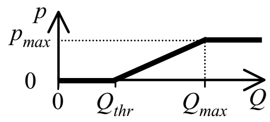
				0.5	1.0	0.4	
B3	1-point	$\frac{slip}{d_0}$	6	$0, \frac{1}{400}, \frac{1}{40}, \frac{1}{4}, \frac{1}{2}, 1$		0.4	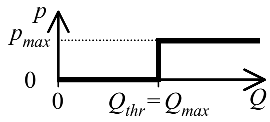
C1	9-point	slip rate [m/s]	5	0.0, 0.001, 0.5, 0.75, 1.0		0.4	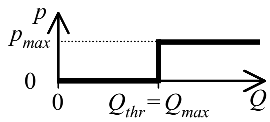
C2	9-point	slip rate [m/s]	2	0.0	0.5	0.4	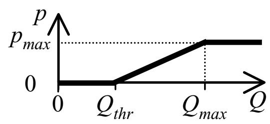
				0.5	1.0	0.4	
C3	9-point	$\frac{slip}{d_0}$	6	$0, \frac{1}{400}, \frac{1}{40}, \frac{1}{4}, \frac{1}{2}, 1$		0.4	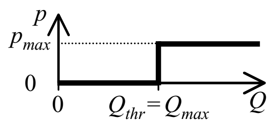
C4 a	9-point	$\frac{slip}{d_0}$	6	0	0 – 5/4 step 1/4	0.4	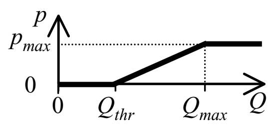
C4 b			11	0	1	0.0 – 1.0, step 0.1	
C4 c			3	$0, \frac{1}{4}, \frac{1}{2}$	1	0.4	

Figure 7. Summary of all tested smoothing algorithms. Algorithm code: A—unconditional averaging on the entire fault plane, B1-B3—threshold condition (TC) applied at one grid point, C1-C4—threshold condition applied at 9 grid points. Q—quantity to which TC is applied, N—the number of tested configurations differing form each other by values of Q_{thr}, Q_{max} and P_{max}, $p(Q)$—the weighting factor as a function of Q.

difficult to estimate value of the slip rate at a point, we know the critical slip in the linear slip-weakening friction law in advance.

Correspondingly, in the C4 algorithm the threshold criterion is applied to the slip-to-critical slip ratio (i.e. this ratio defines Q in C4; as in C3) simultaneously at a point and eight neighbouring gridpoints on the fault, and the averaging parameter p varies linearly from 0 for $Q = Q_{\mathrm{thr}}$ up to p_{max} for $Q = Q_{\mathrm{max}}$. We performed detailed numerical investigation organized in C4a, C4b and C4c sets, see Fig. 7.

Six C4a simulations with $Q_{\mathrm{thr}} = 0$ and $p_{\mathrm{max}} = 0.4$ differ in values of Q_{max}. The results of simulations are illustrated in Fig. 8. It is clear that the grey area is considerably smaller than in the case of algorithms A and B. This means that the scatter of solutions due to different values of Q_{max} is relatively small. The best smoothed solution is the one for $Q_{\mathrm{max}} = 1$. The difference between the rupture times of the smoothed and non-smoothed solutions is about one time step.

Eleven C4b simulations with $Q_{\mathrm{thr}} = 0$ and $Q_{\mathrm{max}} = 1$ differ in values of p_{max}. The results of simulations are illustrated in

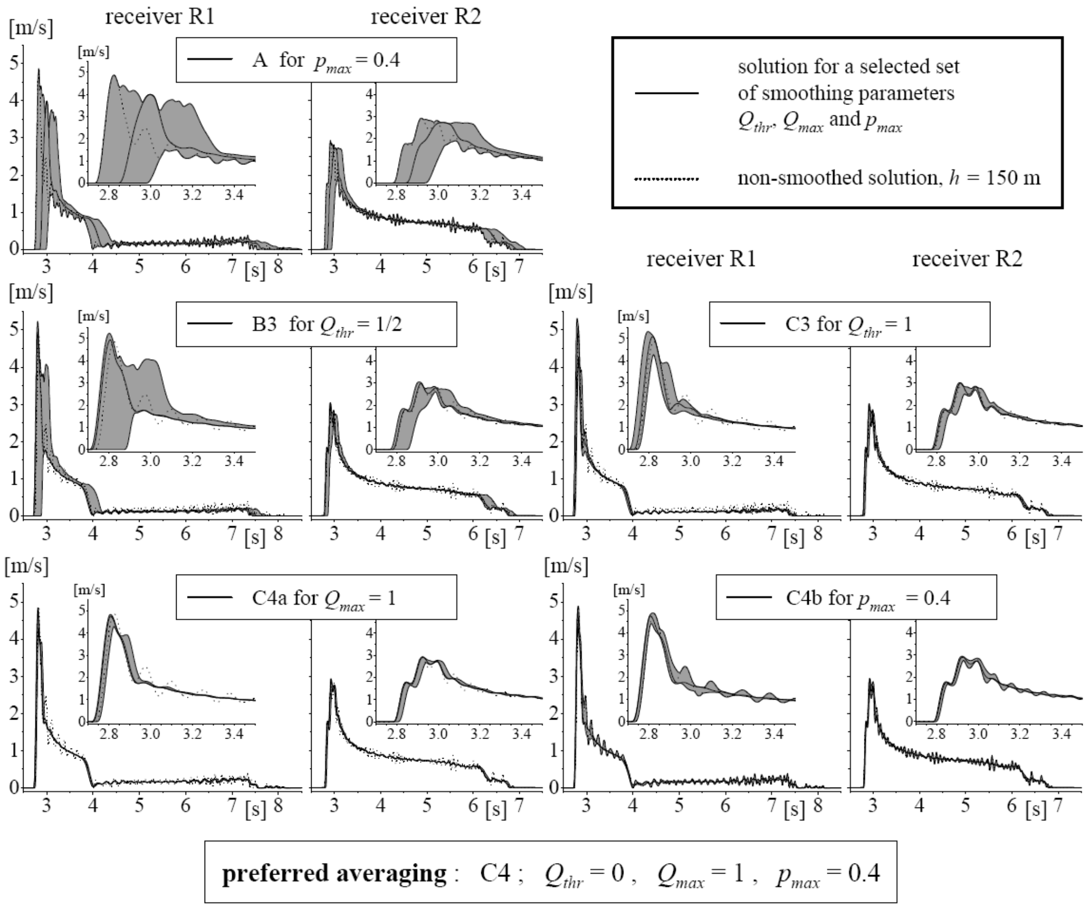

Figure 8. Illustration of numerical results obtained in the process of searching for the best smoothing algorithm. Slip-rate time histories obtained using different tested smoothing algorithms. A, B3, C3 and C4 indicate smoothing algorithms summarized in Fig. 7. Grey area is the area including all considered sets of smoothing parameters; the upper and lower limits of the area at each time are determined by the maximum and minimum slip-rate values from all solutions.

Fig. 8. The scatter in the rupture times for different values of $p_{\max}$ is smaller than the scatter due to different values of $Q_{\max}$ in C4a solutions. The reason why we see some grey area is that the set includes solutions from the non-smoothed ($p_{\max} = 0$) through to the Gaussian-filtered one ($p_{\max} = 1$). The best smoothed solution is the one for $p_{\max} = 0.4$.

Finally, three C4c simulations with $Q_{\max} = 1$ and $p_{\max} = 0.4$ differ in values of $Q_{\rm thr}$. Because the threshold values larger than 0 lead to earlier rupture times compared to the non-smoothed solution, we conclude that the preferred algorithm is C4 with $Q_{\rm thr} = 0$, $Q_{\max} = 1$, and $p_{\max} = 0.4$: the averaging of the trial traction at a gridpoint on the fault is applied if the slip-to-critical slip ratio (this ratio defines Q) is larger than 0 simultaneously at the gridpoint and 8 neighbouring gridpoints on the fault, and the averaging parameter p varies linearly from 0 for $Q = Q_{\rm thr}$ up to $p_{\max}$ for $Q = Q_{\max}$. This algorithm will be applied to Configurations 1 and 2 in the next section.

7 NUMERICAL TESTS FOR THE ADAPTIVE SMOOTHING

Fig. 9 shows development of the breakdown zone during the rupture propagation in the antiplane and in-plane directions for both considered configurations. Recall that the lower curve is determined by the rupture time whereas the upper curve is determined by time when shear traction reaches level of the dynamic friction at the gridpoint. The figure shows results for the non-smoothed simulations with the grid spacing $h = 50$ m. The minimum sizes of the breakdown zone, $\Lambda_{\rm IIImin}$ in the antiplane and $\Lambda_{\rm IImin}$ in the in-plane direction, as well as the corresponding medians $\bar{\Lambda}_{\rm III}$ and $\bar{\Lambda}_{\rm II}$ for both configurations are also given in the figure. We can note that outside the initialization zones, the breakdown zones are narrower in the antiplane directions in both configurations. Therefore, we define the median breakdown-zone resolution $\bar{N}_b$ as the ratio between the median width of the breakdown zone in the antiplane direction and the size of the grid spacing

$$\bar{N}_b = \bar{\Lambda}_{\rm III} / h. \tag{10}$$

We can also note that the rupture time in the initialization zone in Configuration 2 is slightly larger than zero. This is due to the definition of the rupture time (time at which the slip rate first exceeds 1 mm s^{-1}) and relatively slower rupture initialization in Configuration 2. We recall that the size of the initialization zone for Configuration 2 was found by a trial-and-error procedure with a series of numerical simulations with different sizes of the zone and different overshoots because the originally tested zone with the major semi-axis r_a and minor semi-axis r_b determined as critical half-lengths (Andrews 1976a,b) for the in-plane and antiplane directions did not lead to the spontaneous rupture propagation.

Fig. 10 shows rms of differences in the apparent velocities as a function of the grid spacing. The rms measure was determined

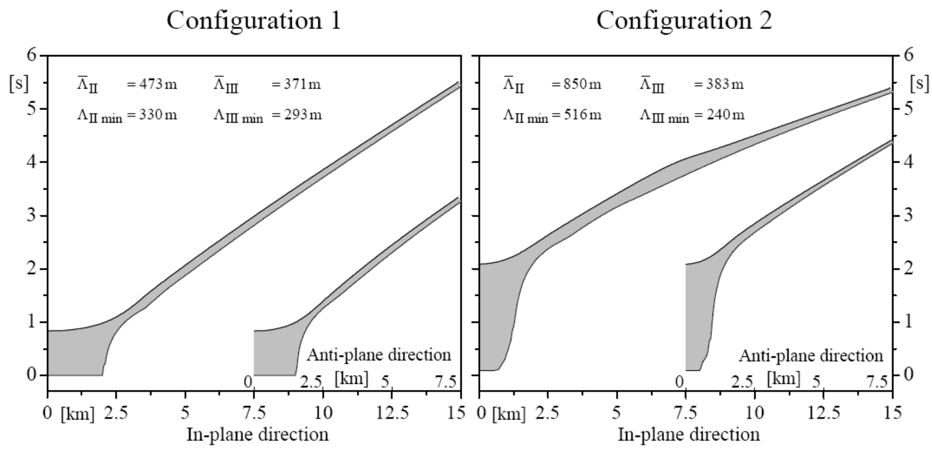

Figure 9. Breakdown zone during rupture propagation along in-plane and antiplane directions in simulations with $h = 50$ m. Minimum and averaged values shown for the in-plane (II) and antiplane (III) propagations.

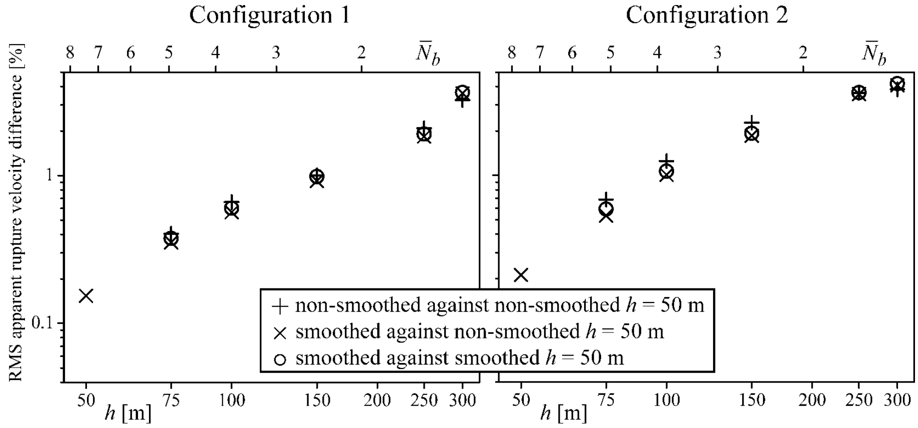

Figure 10. The rms of differences in the apparent velocities determined at the grid positions in the rupture evaluation area shown as a function of the size of grid spacing. The upper axis quantifies the breakdown zone resolution, $\bar{N}_b = \bar{\Lambda}_{III}/h$.

according to eq. (9). The figure displays differences in the apparent velocities for three cases. In the first one, non-smoothed solutions for different h are compared with the non-smoothed solution for $h = 50$ m. The rms differences are shown using symbol '+'. In the second case, smoothed solutions for different h are compared with the non-smoothed solution for $h = 50$ m (see symbol ×). In the third case, smoothed solutions are compared with the smoothed solution for $h = 50$ m (see symbol ∘). We can see that the rms values are smaller than 1 per cent for simulations with $h \leq 100$ m, and the C4 smoothing (with $Q_{\mathrm{thr}} = 0$, $Q_{\mathrm{max}} = 1$, $p_{\mathrm{max}} = 0.4$) practically does not affect the convergence rate. This observation is consistent with our goal to find an algorithm that would only reduce spurious high-frequency oscillations of the slip rate.

Fig. 10 also shows (on the upper horizontal axis) the breakdown-zone spatial resolution defined by eq. (10). Note that $\bar{N}_b$ values for Configurations 1 and 2 were determined for the respective values of $\bar{\Lambda}_{III}$ (therefore they are different for the two configurations). The comparable convergence curves for the two configurations indicate that it was reasonable to define the breakdown-zone spatial resolution for the antiplane direction. This statement can be explained. The medians in the in-plane direction are $\bar{\Lambda}_{II} = 473$ m and $\bar{\Lambda}_{II} = 850$ m for the Configurations 1 and 2, respectively. Similarly, the medians in the antiplane direction are $\bar{\Lambda}_{III} = 371$ and 383 m. If the rms differences in the apparent rupture velocities depended on the spatial sampling of the breakdown zone in the in-plane direction we should see better convergence for Configuration 2. We, however, do not see better convergence. This suggests that the rms difference primarily depends on the spatial sampling of the breakdown zone in the antiplane direction—the medians in the antiplane directions are very close for the two configurations.

For $\bar{N}_b \geq 4$ the rms of differences in the apparent velocities are below 1 per cent.

The rupture propagation is illustrated also in Fig. 11. Each of the frames shows just one quadrant of the rupture area for better visual resolution. This possibility comes with the symmetry of the problem. The figure compares rupture fronts in the smoothed and non-smoothed simulations at discrete times for both configurations and 4 different sizes of the grid spacing h. We can notice slight differences in the rupture front contours near the curve of intersection of the original and bifurcating rupture fronts. Overall, however, the contour plots illustrate that the C4 smoothing (with $Q_{\mathrm{thr}} = 0$, $Q_{\mathrm{max}} = 1$, $p_{\mathrm{max}} = 0.4$) practically does not affect rupture times—the conclusion indicated already by Fig. 10.

We compare smoothed with non-smoothed slip rates in Figs 12(a) and (b) forConfigurations 1 and 2, respectively. The top panel in each figure compares slip rates for four different sizes of the grid spacing h (50, 75, 100 and 150 m) at the antiplane receiver R1,

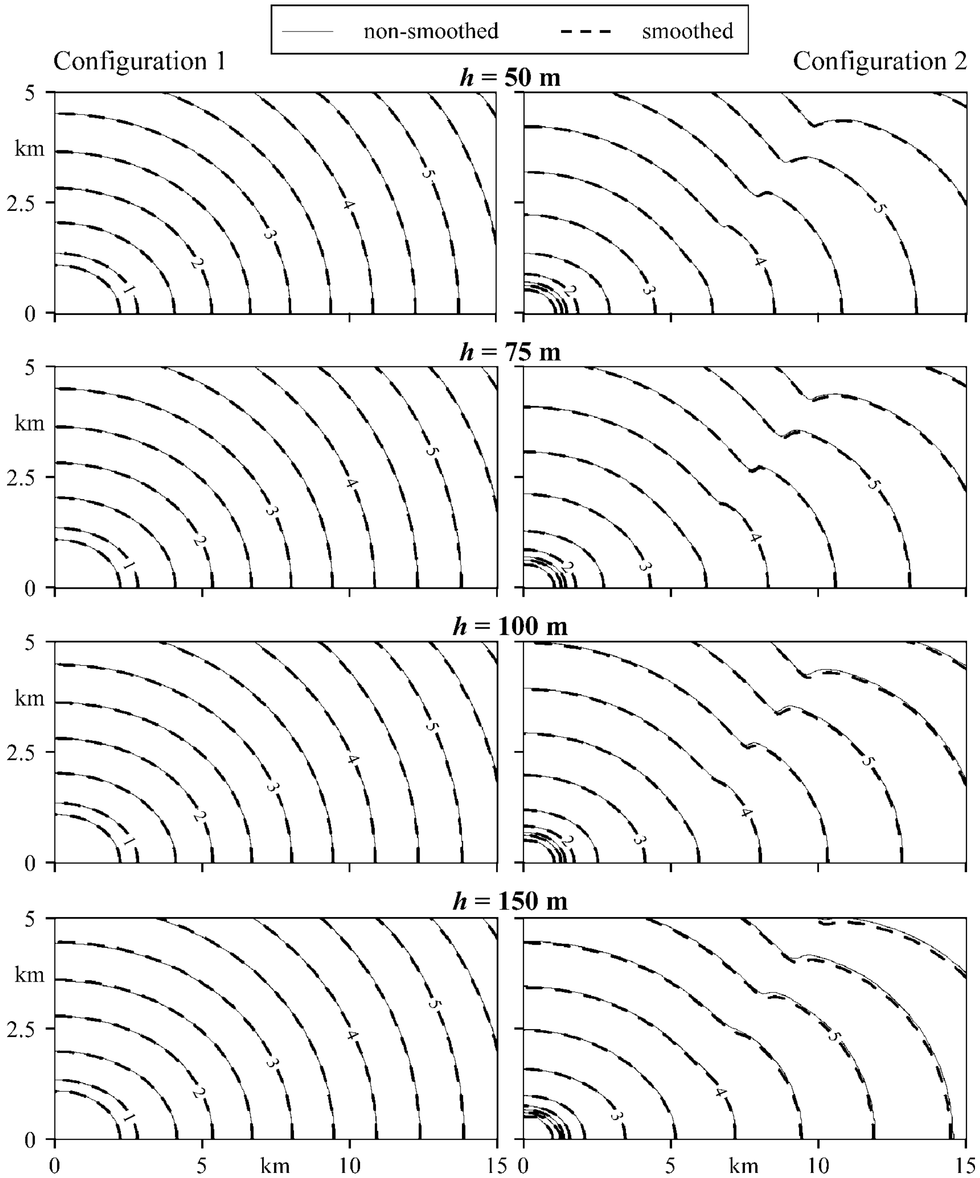

Figure 11. Contour plots of the rupture front shown only in quadrants for better visual resolution. The numbers labelling the contours show rupture times in seconds.

in-plane receiver R2, and mixed-position receiver R3. Note that the y component is different from zero only at R3 and the vertical scale differs from that for the x component. The bottom panel compares smoothed slip rates for 3 different h (75, 100 and 150 m) with the smoothed slip rate for $h = 50$ m.

We can see in the top panels of both figures that the C4 smoothing (with $Q_{\mathrm{thr}} = 0$, $Q_{\mathrm{max}} = 1$, $p_{\mathrm{max}} = 0.4$) effectively reduces spurious high-frequency oscillations in the slip-rate time histories in both problem configurations without affecting the rupture time. The late-time tails are not smoothed as much as the main part of the slip-rate time history. The difference between the smoothness of the main part and the tail is best visible at the antiplane receiver R1. A likely explanation is that the smoothing does not sufficiently reduce corresponding frequencies which are lower than the frequencies of the spurious oscillations in the main part of the slip-rate time histories.

The bottom panel clearly shows that the smoothness of solutions for $h = 75,\ 100$ and 150 m is close to that of the solution for $h = 50$ m. Overall, the smoothed slip rates for all h in Configuration 1 are close, although slight differences appear with the increasing h. In Configuration 2, however, we can see considerably increasing differences with increasing h. Because we can see analogous differences between the non-smoothed slip rates for different values of h in the top panel of Fig. 12(b), it is obvious that the differences are not due to the applied smoothing algorithm. The differences between smoothed or non-smoothed solutions for different values of h are most likely due to the TSN algorithm itself.

Fig. 13 shows the fault shear traction as a function of time for the slip rates obtained for Configurations 1 and 2 with $h = 150$ m. The columns of the figure correspond to those in Figs 12(a) and (b). Curves in red show the fault shear traction in the non-smoothed solutions, curves in black show the fault shear traction in the smoothed solutions. We can see that the application of the adaptive smoothing algorithm does not cause error in the shear traction. Small visible differences between the tractions in the smoothed and non-smoothed

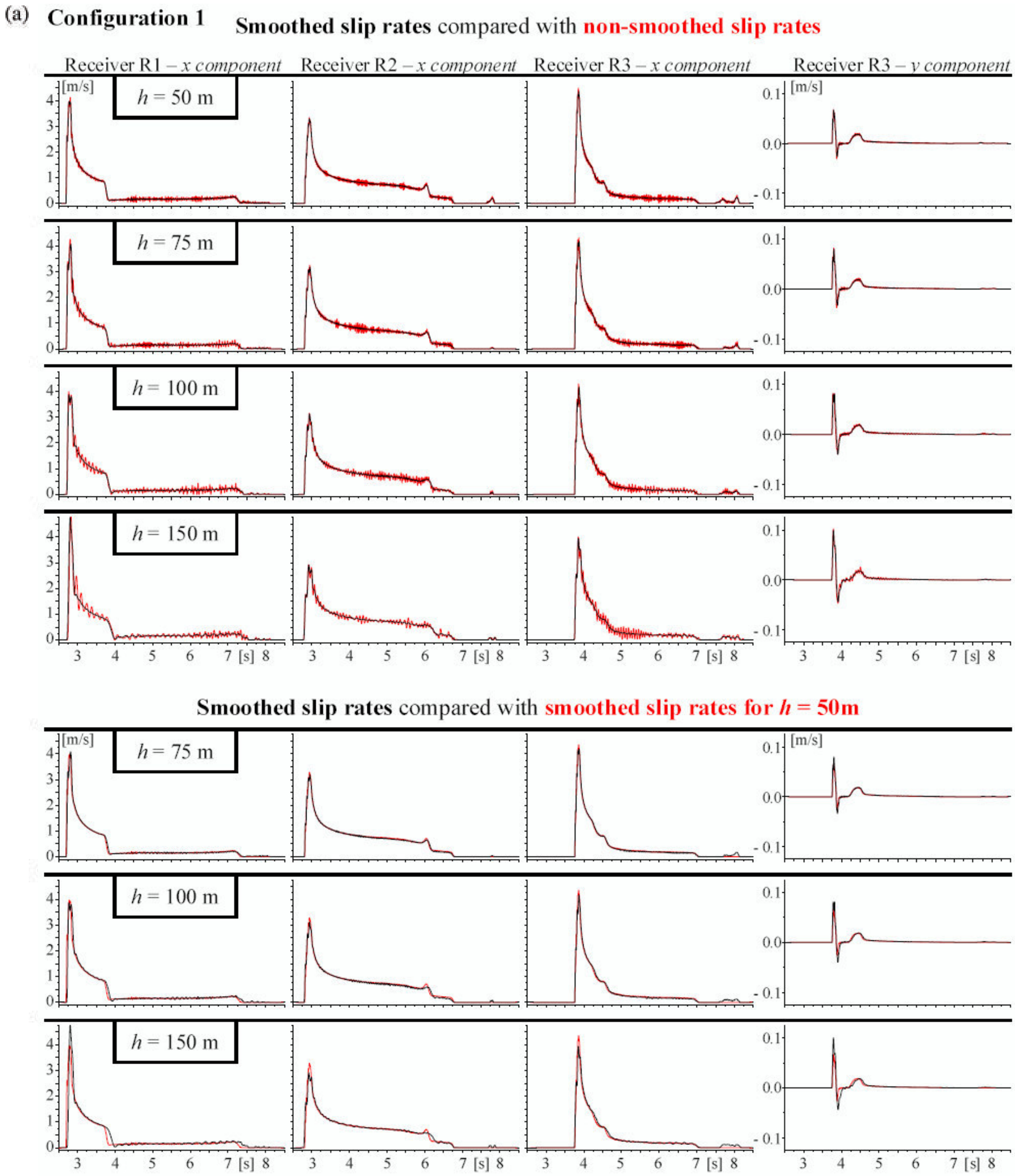

Figure 12. (a) Slip-rate time histories for Configuration 1. (b) Slip-rate time histories for Configuration 2.

solutions at the mixed-position receiver R3 are very likely due to the fact that the receiver is located close to the line along which the rupture front bifurcates. As we previously mentioned, the lines slightly differ in position in the smoothed and non-smoothed solutions. Note however, that we show the coarsest spatial discretization. The level of agreement is better in finer discretizations ($h = 50,\ 75$ and 100).

8 CONCLUSIONS

We have developed an adaptive smoothing algorithm for reducing spurious high-frequency oscillations of the slip-rate time histories in the FE–traction-at-split-node modelling of dynamic rupture propagation on planar faults with the linear slip-weakening friction law. The algorithm spatially smoothes trial traction on the fault. The smoothed value of the trial traction at the gridpoint (i, j), at a given time level, is obtained as a weighted average of the Gaussian-filtered and unfiltered values

$$\bar{\vec{T}}(i, j) = \sum_{k=1}^{3} \sum_{l=1}^{3} \bar{w}_{kl}\, \vec{T}(i + k - 2, j + l - 2). \tag{11}$$

Here $\vec{T}$ denotes the original value of the trial traction,

$$\bar{w} \;=\; \begin{bmatrix} p/16 & p/8 & p/16 \\ p/8 & 1 - 3p/4 & p/8 \\ p16 & p/8 & p/16 \end{bmatrix}, \tag{12}$$

and p varies during slip development linearly from 0 for zero slip up to $p_{\max} = 0.4$ for the critical slip value. The averaging formula (11)

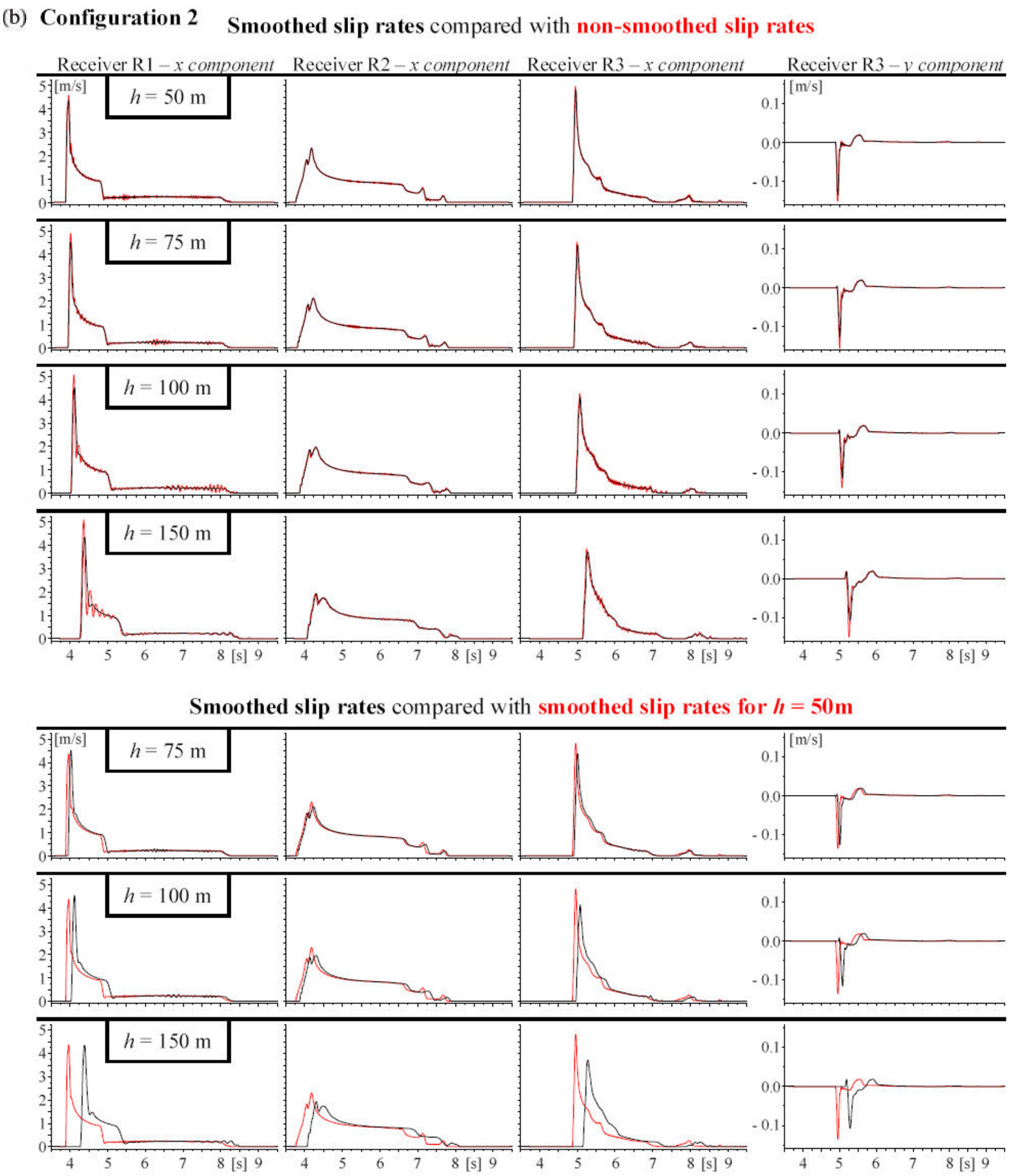

Figure 12. (*Continued.*)

is applied if the slip is larger than 0 simultaneously at the gridpoint (i, j) and eight neighbouring gridpoints on the fault.

Extensive numerical tests demonstrate that the adaptive smoothing algorithm effectively reduces spurious high-frequency oscillations of the slip-rate time histories without affecting rupture time. The smoothing algorithm is a purely numerical tool.

We implemented the smoothing algorithm in the FE part of the 3-D hybrid FD–FE method. This makes it possible to simulate dynamic rupture propagation inside a FE subdomain surrounded by the FD subdomain covering major part of the whole computational domain.

Finally, we conclude with remarks on possible extensions. In all performed simulations we assumed a uniform grid on the fault. This allowed using the same weighting coefficients in the averaging formula at all gridpoints. In principle it should not be a problem to determine weighting coefficients in the case of a non-uniform grid.

As stated in the introduction, the traction-at-split-node method has been implemented in various FD schemes. We assume that the presented algorithm or some slightly modified algorithm should work also with the FD implementations.

The two possible extensions and generalizations require further separate studies.

ACKNOWLEDGMENTS

We very much appreciate discussion with Steve Day. Reviews by Steve Day, Ruth Harris and two anonymous reviewers considerably helped to improve the presentation. This work was supported in

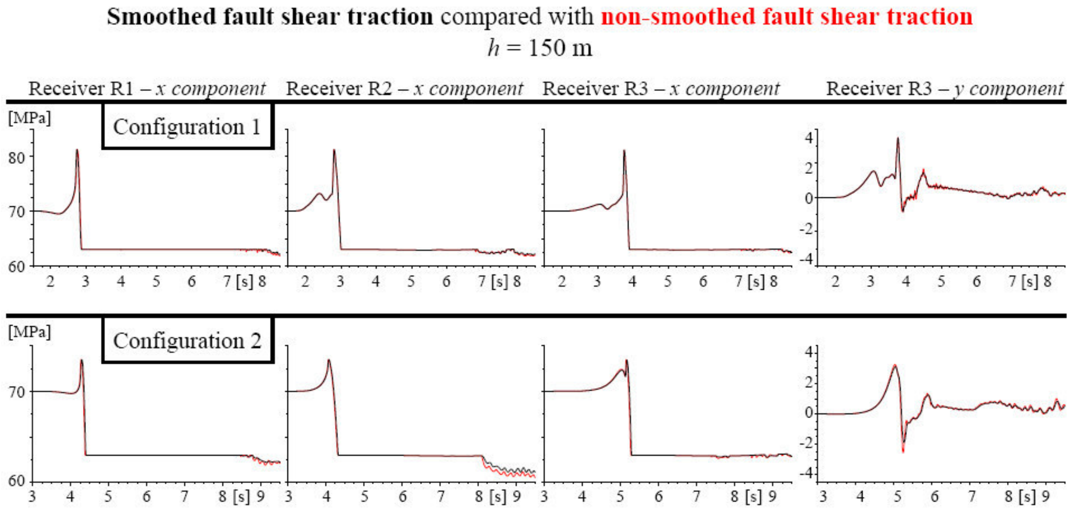

Figure 13. Fault shear traction in smoothed and non-smoothed solutions for two configurations obtained with $h = 150$ m.

part by the Slovak Research and Development Agency under the contract No. APVV-0435–07 (project OPTIMODE), the Scientific Grant Agency of the Ministry of Education of the Slovak Republic and the Slovak Academy of Sciences (VEGA) Project 1/4032/07, and the ITSAK-GR MTKD-CT-2005–029627 Project.

REFERENCES

Aagaard, B., Heaton, T.H. & Hall, J.F., 2001. Dynamic earthquake ruptures in the presence of lithostatic normal stresses: implications for friction models and heat production, *Bull. seism. Soc. Am.,* **91,** 1765–1796.

Ampuero, J.-P., 2002. Etude physique et numerique de la nucleation des seismes, *PhD. thesis*. Universite Paris 7, Denis Diderot.

Ampuero, J.-P., 2008. SEM2DPACK: a spectral element method for 2D wave propagation and earthquake source dynamics, version 2.3.3, available at http://sourceforge.net/projects/sem2d/.

Anderson, G., Aagaard, B. & Hudnut, K., 2003. Fault interactions and large complex earthquakes in the Los Angeles area, *Science,* **302,** 1946–1949.

Andrews, D.J., 1973. A numerical study of tectonic stress release by underground explosions, *Bull. seism. Soc. Am.,* **63,** 1375–1391.

Andrews, D.J., 1976a. Rupture propagation with finite stress in antiplane strain, *J. geophys. Res.,* **81,** 3575–3582.

Andrews, D.J., 1976b. Rupture velocity of plane strain shear cracks, *J. geophys. Res.,* **81,** 5679–5687.

Andrews, D.J., 1985. Dynamic plane-strain shear rupture with a slip weakening friction law calculated by a boundary integral method, *Bull. seism. Soc. Am.,* **75,** 1–21.

Andrews, D.J., 1999. Test of two methods for faulting in finite-difference calculations, *Bull. seism. Soc. Am.,* **89,** 931–937.

Aochi, H., Fukuyama, E. & Matsu'ura, M., 2000. Selectivity of spontaneous rupture propagation on a branched fault, *Geophys. Res. Lett.,* **27,** 3635–3638.

Archuleta, R.J., 1976. Experimental and numerical three-dimensional simulations of strike-slip earthquakes, *PhD thesis*. University of California, San Diego.

Archuleta, R.J. & Frazier, G.A., 1978. Three-dimensional numerical simulations of dynamic faulting in a half-space, *Bull. seism. Soc. Am.,* **68,** 541–572.

Balazovjech, M. & Halada, L., 2007. Effective computation of restoring force vector in FEM, *Kybernetika,* **43,** 767–776.

Chaljub, E., Komatitsch, D., Vilotte, J.P., Capdeville, Y. & Festa, G., 2007. Spectral Element Analysis in Seismology, in *Advances in Wave Propagation in Heterogeneous Earth,* Vol. 48: Advances in Geophysics, pp. 365–420, eds Wu, R.-S., Maupin, V. & Dmowska, R., Elsevier/Academic Press, San Diego.

Cochard, A. & Madariaga, R., 1994. Dynamic faulting under rate dependent friction, *Pure appl. Geophys.,* **105**(25), 891–907.

Cruz-Atienza, V.M. & Virieux, J., 2004. Dynamic rupture simulation of non-planar faults with a finite-difference approach, *Geophys. J. Int.,* **158,** 939–954.

Dalguer, L.A. & Day, S.M., 2006. Comparison of fault representation methods in finite difference simulations of dynamic rupture, *Bull. seism. Soc. Am.,* **96,** 1764–1778.

Dalguer, L.A. & Day, S.M., 2007. Staggered-grid split-node method for spontaneous rupture simulation, *J. geophys. Res.,* **112,** B02302, doi:10.1029/2006JB004467.

Das, S., 1980. A numerical method for determination of source time functions for general three-dimensional rupture propagation, *Geophys. J. R. astr. Soc.,* **62,** 591–604.

Day, S.M., 1977. Finite element analysis of seismic scattering problems, PhD thesis, University of California, San Diego.

Day, S.M., 1982. Three-dimensional simulation of spontaneous rupture: the effect of nonuniform prestress, *Bull. seism. Soc. Am.,* **72,** 1881–1902.

Day, S.M., Dalguer, L.A., Lapusta, N. & Liu, L., 2005. Comparison of finite difference and boundary integral solutions to three-dimensional spontaneous rupture, *J. geophys. Res.,* **110,** B12307, doi:10.1029/2005JB003813.

Festa, G., 2004. Slip imaging by isochron back projection and source dynamics with spectral element methods, *Tesi di Dottorato in Geofisica,* Universita degli studi di Bologna.

Galis, M., Moczo P. & Kristek, J., 2008. A 3-D hybrid finite-difference—finite-element viscoelastic modeling of seismic wave motion, *Geophys. J. Int.,* **175,** 153–184, doi:10.1111/j.1365-246X.2008.03866.x.

Harris, R.A. & Archuleta, R., 2004. Earthquake rupture dynamics: comparing the numerical simulation methods, *EOS, Trans. Am. geophys. Un.,* **85**(34), 321.

Harris, R.A. *et al*., 2004. The Source Physics of Large Earthquakes – Validating Spontaneous Rupture Methods, *EOS, Trans. Am. goephys. Un.,* **85**(47), Fall Meet. Suppl., Abstract S12A-05.

Harris, R.A. *et al*., 2009. The SCEC/USGS Dynamic earthquake rupture code verification exercise, *Seismol. Res. Lett.,* **80,** 119–126.

Kaneko, Y., Lapusta, N. & Ampuero, J.-P., 2008. Spectral element modeling of spontaneous earthquake rupture on rate and state faults: effect of velocity-strengthening friction at shallow depths, *J. geophys. Res.,* **113,** B09317, doi:10.1029/2007JB005, 553.

Lapusta, N. & Rice, J.R., 2003. Nucleation and early seismic propagation of small and large events in a crustal earthquake model, *J. geophys. Res.,* **108**(B4), 2205, doi:10.1029/2001JB000793.

Lapusta, N., Rice, J.R., Ben-Zion, Y. & Zheng, G., 2000. Elastodynamic analysis for slow tectonic loading with spontaneous rupture episodes on faults with rate- and state-dependent friction, *J. geophys. Res.,* **105,** 23 765–23 789.

Ma, S., 2008. A physical model for widespread near-surface and fault zone damage induced by earthquakes, *Geochem. Geophys. Geosyst.,* **9,** Q11009, doi:10.1029/2008GC002231.

Ma, S. & Archuleta, R.J., 2006. Radiated seismic energy based on dynamic rupture models of faulting, *J. geophys. Res.* **111,** B05315, doi:10.1029/2005JB004055.

Ma, S. & Liu, P., 2006. Modeling of the perfectly matched layer absorbing boundaries and intrinsic attenuation in explicit finite-element methods, *Bull. seism. Soc. Am.,* **96,** 1779–1794, doi:10.1785/0120050219.

Ma, S., Custódio, S., Archuleta, R.J. & Liu, P., 2008. Dynamic modeling of the 2004 Mw 6.0 Parkfield, California, earthquake, *J. geophys. Res.,* **113,** B02301, doi:10.1029/2007JB005216.

Madariaga, R., 1976. Dynamics of an expanding circular fault, *Bull. seism. Soc. Am.,* **67,** 163–182.

Madariaga, R., Olsen, K. & Archuleta, R., 1998. Modeling dynamics rupture in a 3D earthquake fault model, *Bull. seism. Soc. Am.,* **88,** 1182–1197.

Miyatake, T., 1980. Numerical simulations of earthquake source process by a three-dimensional crack model. Part 1: rupture process, *J. Phys. Earth,* **28,** 565–598.

Moczo, P., Ampuero, J.-P., Kristek, J., Gális, M., Day, S.M. & Igel, H., 2005. The European Network SPICE Code Validation, *EOS, Trans. Am. geophys. Union,* **86**(52), Fall Meet. Suppl., Abstract S13A-0180.

Moczo, P., Ampuero, J.-P., Kristek, J., Day, S.M., Kristekova, M., Pazak, P., Galis, M. & Igel, H., 2006. Comparison of numerical methods for seismic wave propagation and source dynamics—the SPICE Code Validation, in ESG 2006, in *Third Int. Symposium on the Effects of Surface Geology on Seismic Motion,* Vol. 1, pp. 495–504, eds P.-Y. Bard, *et al*., Grenoble.

Moczo, P., Kristek, J., Galis, M., Pazak, P. & Balazovjech, M., 2007a. The finite-difference and finite-element modeling of seismic wave propagation and earthquake motion, *Acta Phys. Slovaca* **57,** 177–406.

Moczo, P., Robertsson, J.O.A. & Eisner, L., 2007b. The finite-difference time-domain method for modeling of seismic wave propagation, in *Advances in Wave Propagation in Heterogeneous Earth,* Vol. 48: Advances in Geophysics, pp. 421–516, eds Wu, R.-S., Maupin, V. & Dmowska, R., Elsevier/Academic Press, San Diego.

Nielsen S., Carlson, J.M. & Olsen, K., 2000. Influence of friction and fault geometry on earthquake rupture, *J. geophys. Res.,* **105B,** 6069–6088.

Oglesby, D.D., 1999. Earthquake dynamics on dip-slip faults, *PhD. thesis*. University of California, Santa Barbara.

Oglesby, D.D., Archuleta, R.J. & Nielsen, S.B., 1998. Earthquakes on dipping faults: the effects of broken symmetry, *Science,* **280,** 1055–1059.

Oglesby, D.D., Archuleta, R.J. & Nielsen, S.B., 2000. The three-dimensional dynamics of dipping faults, *Bull. seism. Soc. Am.,* **90,** 616–628.

Ohnaka, M. & Yamashita T., 1989. A cohesive zone model for dynamic shear faulting based on experimentally inferred constitutive relation and strong motion source parameters, *J. geophys. Res.,* **94,** 4089–4104.

Rojas, O., Day, S.M., Castillo, J. & Dalguer, L.A., 2008. Modelling of rupture propagation using high-order mimetic finite differences, *Geophys. J. Int.,* **172,** 631–650.

Rojas, O., Dunham, E., Day, S.M., Dalguer, L.A. & Castillo, J., 2009. Finite difference modeling of rupture propagation with strong velocity-weakening friction, *Geophys. J. Int.,* submitted.

Vilotte, J.-P., Festa, G. & Ampuero, J.-P., 2006. Dynamic fault rupture propagation using nonsmooth spectral element method, *EOS, Trans. Am. geophys. Union,* **87**(52), Fall Meet. Suppl., Abstract S52B–05.